

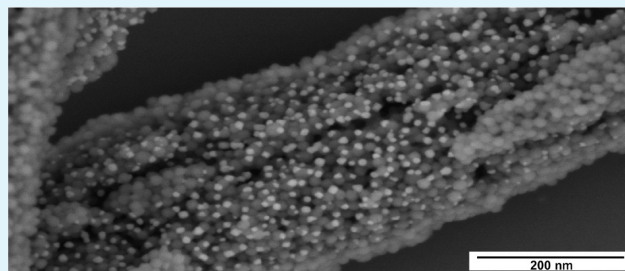
Hierarchically Structured Metal Oxide/Silica Nanofibers by Colloid Electrospinning

Nesrin Horzum,^{†,‡} Rafael Muñoz-Espí,[†] Gunnar Glasser,[†] Mustafa M. Demir,^{‡,§} Katharina Landfester,[†] and Daniel Crespy^{*,†}

[†]Max Planck Institute for Polymer Research, Ackermannweg 10, 55128 Mainz, Germany

[‡]Department of Chemistry, and [§]Material Science and Engineering Program, Izmir Institute of Technology, Urla, 35430, İzmir, Turkey

ABSTRACT: We present herein a new concept for the preparation of nanofibrous metal oxides based on the simultaneous electrospinning of metal oxide precursors and silica nanoparticles. Precursor fibers are prepared by electrospinning silica nanoparticles (20 nm in diameter) dispersed in an aqueous solution of poly(acrylic acid) and metal salts. Upon calcination in air, the poly(acrylic acid) matrix is removed, the silica nanoparticles are cemented, and nanocrystalline metal oxide particles of 4–14 nm are nucleated at the surface of the silica nanoparticles. The obtained continuous silica fibers act as a structural framework for metal oxide nanoparticles and show improved mechanical integrity compared to the neat metal oxide fibers. The hierarchically nanostructured materials are promising for catalysis applications, as demonstrated by the successful degradation of a model dye in the presence of the fibers.



KEYWORDS: catalysis, ceria, electrospinning, lithium cobalt oxide, metal oxide, nanoparticles

INTRODUCTION

Because of their large ratio of surface area to volume and interconnected porosity, metal oxide meshes have been proposed for applications in catalysis, energy storage, and sensors.^{1–3} Various bottom-up approaches—such as vapor–liquid–solid (VLS)⁴ and vapor–solid (VS)⁵ growth—and top-down techniques—such as nanocarving⁶ and electrospinning⁷—have been described. Among these techniques, electrospinning is probably the most versatile, because it allows the fabrication of fibrous mats from a wide variety of both organic and/or inorganic materials.^{8,9} Moreover, it allows for control over the diameter, morphology, porosity, alignment, and composition of the resulting fibers.^{10,11}

Calcination of electrospun mats obtained from metal oxide precursors is a commonly used approach because of its facility and potential for upscaling. The calcination process is usually applied to mixtures of polymers/metal oxide precursors and it is based on an oxidative conversion of the polymeric component by heat treatment. There are many successful examples in literature for the fabrication of inorganic fibers by calcination of precursor materials prepared by sol–gel,^{12–18} polymer-based sol–gel processes,^{19–22} or from electrospinning of polymer dispersions in the presence of ex situ formed colloids.^{23–27} Upon increase of the temperature, metal oxide crystals nucleate and grow while the polymeric component undergoes degradation.^{28,29}

In the electrospinning of inorganic precursor, one has to take into account that the calcination leads almost automatically to a shrinkage of the fibers because the polymer template is

removed. After calcination, the nanofibers are usually more brittle³⁰ because of their thinner section and the internal stress generated by the shrinkage. Therefore, an additional material that is not mechanically or chemically affected by the calcination process needs to be incorporated in the fibers during the electrospinning.

The recently reviewed electrospinning of colloids³¹ has been explored for the fabrication of metal or metalloid oxide fibers. For instance, silica^{24,26} and titania³² nanoparticles were embedded in polymer fibers by electrospinning a solution of polymer template in the presence of a dispersion of the particles. Recently, the electrospinning of a zinc powder/titanium isopropoxide/poly(vinyl acetate) mixture was reported.³³ The precursor fibers were calcinated in air and the subsequent hydrothermal treatment of the resulting fibers in bis(hexamethylene)tri-amine and a zinc nitrate hexahydrate solution yielded continuous TiO₂ fibers decorated with ZnO branches. The ZnO particles in the TiO₂ fibers seeded the growth of ZnO branches perpendicular to the TiO₂ fibers direction. The same procedure was employed to form ZnO-branched Co₃O₄³⁴ and ZnO-branched ZnO³⁵ fibers. Although the synthesis of silica-supported metal oxide nanocomposites has been previously reported,^{36–38} their fabrication by colloid-electrospinning to obtain nanofibers is a new strategy. Our concept allows the advantageous combination of interesting

Received: September 12, 2012

Accepted: October 23, 2012

Published: October 23, 2012

properties inherent to both nanoparticles (high surface area) and meshes (porous structure and facile separation from the reaction media). Furthermore, the incorporation of silica nanoparticles in the composite fibers significantly improves the mechanical integrity of the nanofibers. The generality of the concept is demonstrated by taking two different metal oxides, namely CeO₂ and LiCoO₂ as models for simple and binary oxides, respectively. The catalytic activity of the composite nanofibers was also investigated.

EXPERIMENTAL SECTION

Materials. Cerium(III) nitrate hexahydrate (Fluka, ≥99.0%), lithium hydroxide (Aldrich, 98%), cobalt(II) hydroxide (Aldrich, 95%), poly(acrylic acid) (PAA, $M_w \approx 450\,000\text{ g mol}^{-1}$, Polysciences Inc.), colloidal silica (average diameter: 20 nm, BET surface area: $140\text{ m}^2\text{ g}^{-1}$, 34 wt % suspension in H₂O, Sigma-Aldrich), and rhodamine B (Merck) were all used as received without any further purification. Demineralized water was used throughout the study.

Preparation of the Electrospinning Solutions. The metal salt(s), Ce(NO₃)₃·6H₂O (780 mg, 1.8 mmol; and 390 mg, 0.9 mmol) or LiOH (21.5 mg, 0.9 mmol) and Co(OH)₂ (83 mg, 0.90 mmol), were added to a 7.5 wt % solution of PAA (0.870 g), and the mixture was stirred for 2 h at room temperature.

For the fabrication of metal oxide/silica fibers, the colloidal silica was dispersed in 4.0 g of the PAA/metal salt solution. The weight ratio of PAA:SiO₂ was fixed as 1:1. Two different Ce(NO₃)₃·6H₂O concentrations with respect to the amount of silica (mole ratios Ce:Si) were used: 0.06:1.00 and 0.12:1.00 (mole ratios).

Fabrication of the Nanofibers. The viscous solutions of PAA/metal salt precursor or the dispersions of PAA/metal salt precursor/SiO₂ were loaded in a plastic syringe connected with silicon rubber tubing. The electrospinning experiments were carried out with a commercial platform (ES1a, Electrospinz) covered with a polycarbonate box placed for safety and to avoid disturbances from air convection. The positive electrode was applied to the spinneret and an aluminum foil was used as counter electrode. The flow rate of the polymer solution was adjusted by a syringe pump (Bibblock, K₄ Scientific). The optimum electrospinning parameters are presented in Table 1. PAA/SiO₂, PAA/SiO₂/Ce(NO₃)₃, PAA/Ce(NO₃)₃, and

Table 1. Optimized Electrospinning Parameters (tip-to-collector distance fixed at 14 cm)

metal oxide	precursor	electric field (kV cm ⁻¹)	flow rate (mL h ⁻¹)
CeO ₂	PAA/Ce(NO ₃) ₃ ·6H ₂ O	0.71	2
CeO ₂ /SiO ₂	PAA/Ce(NO ₃) ₃ ·6H ₂ O/SiO ₂	0.71	2
SiO ₂	PAA/SiO ₂	0.36	1
LiCoO ₂	PAA/LiOH/Co(OH) ₂	1.43	2
LiCoO ₂ /SiO ₂	PAA/LiOH/Co(OH) ₂ /SiO ₂	0.71	1

PAA/SiO₂/LiOH/Co(OH)₂ fibers were calcinated under air in a muffle oven (Nabertherm Controller P330 LT S/13) at 600 °C (room temperature to 600 °C at a rate of 4 °C min⁻¹; plateau of 2 h at 600 °C). PAA/LiOH/Co(OH)₂ fibers were calcinated at 400 °C for 5 h with a rate of 4 °C min⁻¹.

Characterization Methods. The fibers were electrospun onto silicon wafers for morphological observations by scanning electron microscopy (SEM) in a LEO 1530 Gemini microscope (Zeiss). To localize the metal oxide nanoparticles on the fibers, high-resolution SEM micrographs were captured using a Hitachi SU8000 microscope. The diameter of fibers and particle size distributions were calculated from SEM micrographs by using the software Fiji/ImageJ. X-ray diffraction pattern (XRD) were recorded in a Philips PW 1820 diffractometer using Cu_{Kα} radiation ($\lambda = 1.5418\text{ \AA}$). Thermogravimetric analysis (TGA) was studied by a Mettler Toledo 851

thermobalance. The specific surface area of the calcinated fibers was determined from nitrogen adsorption using a Micromeritics Gemini V instrument. The surface area was calculated according to the Brunauer–Emmett–Teller (BET) methodology (five point, $0.05 < P/P_0 < 0.3$). The samples were degassed at 400 °C for 6 h in vacuum prior to the measurements.

The photocatalytic degradation of rhodamine B (Merck) in the presence of pure CeO₂, CeO₂/SiO₂, and SiO₂ fibers was carried out in a polystyrene plate (Corning) under UV light irradiation. For the catalysis experiments, the fiber catalyst (2.0 mg) was added to an aqueous solution of rhodamine B (1.5 mL, 5 ppm) and stirred continuously. At certain time intervals, photoluminescence (PL) emission spectra of the dye solution with the fiber mats were registered in top-mode on a Tecan Infinite M100 plate reader using an excitation wavelength of 500 nm.

RESULTS AND DISCUSSION

The preparation of silica-supported metal oxide fibers by colloidal electrospinning and subsequent controlled thermal treatment is presented for two systems: CeO₂, as a model for a simple metal oxide, and LiCoO₂, as a model for a binary system. Silica nanoparticles were selected as cheap but robust structural framework for the final materials. Initially, poly(acrylic acid) (PAA) and a metal salt (either Ce(NO₃)₃·6H₂O or LiOH and Co(OH)₂) were dissolved in water, and the homogeneous aqueous polymer solution was electrospun. In a second step, the resulting mats were converted to metal oxide fibers by thermal treatment in a controlled environment. A schematic diagram for the fabrication of metal oxide and metal oxide/silica fibers is depicted in Figure 1. In both systems, PAA was used as polymer template and binder in the fibers. PAA is a commonly used polyelectrolyte, with most of the carboxyl groups being deprotonated at neutral pH ($pK_a\ 4\text{--}4.5$),³⁹ which provide the ability to coordinate metal cations.

The thermal decomposition of PAA/SiO₂ fibers measured by thermogravimetric analysis (TGA) showed two consecutive mass losses (Figure 2a), attributed to the elimination of adsorbed water, and to the degradation of poly(acrylic acid).⁴⁰ The three weight losses observed for the PAA/Ce(NO₃)₃ and PAA/Ce(NO₃)₃/SiO₂ fibers are consecutive to the elimination of adsorbed water, the dehydration of cerium nitrate and degradation of PAA, and the conversion of anhydrous Ce(NO₃)₃ to CeO₂ (at increasing temperature).⁴¹ Since the mass of the materials remains unchanged around 600 °C, the calcination temperature was fixed at this temperature. After calcination, the majority of the remaining residue is expected to be composed of CeO₂ and/or SiO₂. Experimentally measured and theoretical percentages of remaining residues, calculated from the initially introduced precursor assuming complete conversion to CeO₂, are listed in Table 2. In the presence of SiO₂ nanoparticles, the remaining material after calcination of PAA/SiO₂ fibers was higher (48%) than that of PAA/Ce(NO₃)₃ fibers (23%). The thermal stability of the fibers was slightly increased upon addition of SiO₂ nanoparticles with an onset of degradation temperature shifted to more than 15 °C in the presence of silica particles.

Similarly, the thermal decomposition of the PAA/LiOH/Co(OH)₂ fibers occurs in three stages in the temperature range of 25–720 °C (Figure 2b). The weight losses were ascribed to the removal of adsorbed water (~10%), the polymer degradation and the conversion of Co(OH)₂ to Co₃O₄ (56%),⁴² and the reaction of Co₃O₄ with the lithium salt to form LiCoO₂.⁴³ Similar to the aforementioned results obtained for CeO₂, the addition of SiO₂ nanoparticles shifted the

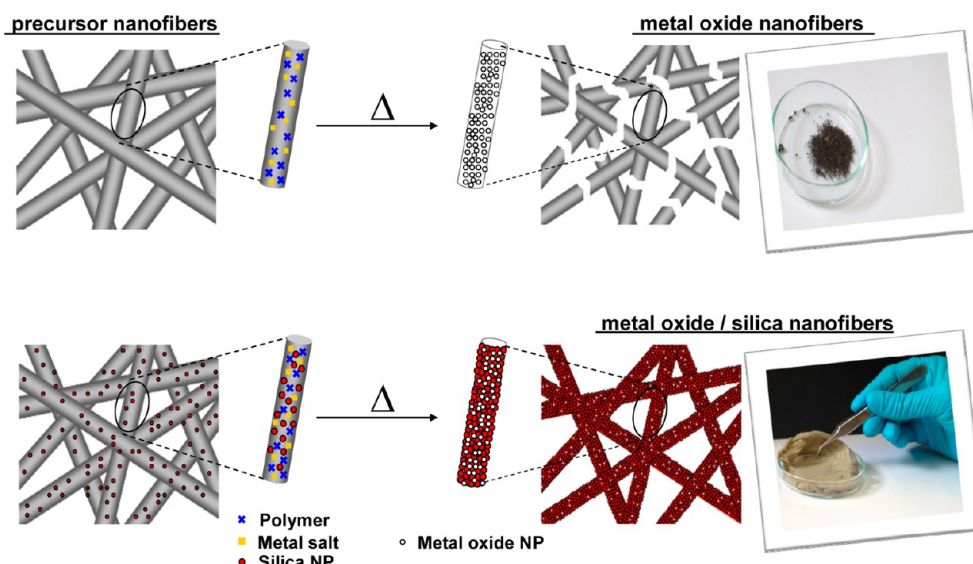


Figure 1. Scheme of the preparation of metal oxide (top) and metal oxide/silica (bottom) fibers. The metal oxide fibers are brittle and yield a powder material, whereas the nanofibrous morphology is conserved by using silica nanoparticles as structural framework.

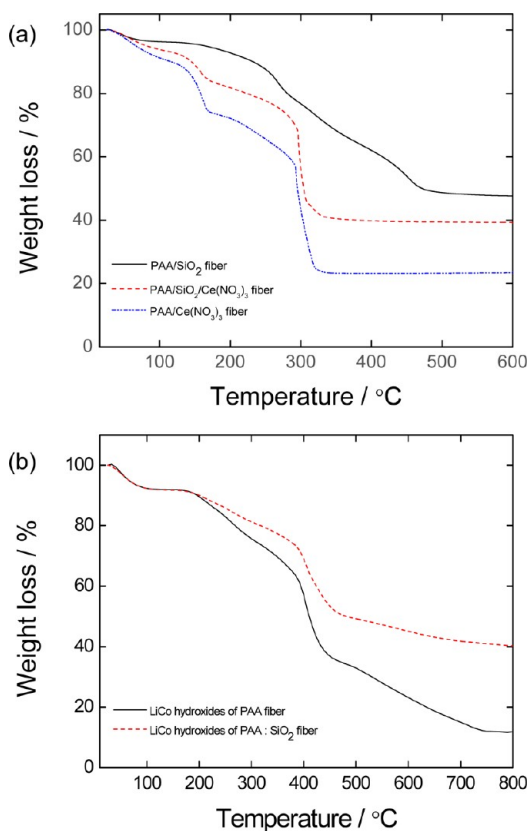


Figure 2. TGA thermograms of (a) PAA/SiO₂/Ce(NO₃)₃ and PAA/Ce(NO₃)₃ fibers, and (b) PAA/LiOH/Co(OH)₂, PAA/SiO₂/LiOH/Co(OH)₂ fibers.

decomposition temperature to higher values. Indeed, the remaining mass at 600 °C for the PAA/LiCo hydroxide fibers was 23% versus 45% in the presence of 6.5 wt % of SiO₂. Since the degradation mechanism relies generally on the diffusion of polymer residues formed upon increase of temperature, the nanoparticles may act as barrier for mass transport, hence improving the thermal properties of the materials. Such phenomenon was already reported by Mizuno et al.,⁴⁴ who

Table 2. Diameters of the Fibers and Percent Compositions of the Metal Oxide/Silica Fibers

fiber	d_{fiber} before calcination ^a (nm)	d_{fiber} after calcination ^a (nm)	CeO ₂ ^b (vol %)	CeO ₂ + SiO ₂ ^c (wt %)	CeO ₂ + SiO ₂ ^d (wt %)
SiO ₂	540 ± 80	510 ± 80		48	50
CeO ₂ /SiO ₂ (0.06/1.00)	290 ± 50	180 ± 30	6.3	40	48
CeO ₂ /SiO ₂ (0.12/1.00)	300 ± 40	190 ± 30	12.2	33	47
CeO ₂	320 ± 50	240 ± 40	100.0	23	19
fiber	d_{fiber} before calcination ^a (nm)	d_{fiber} after calcination ^a (nm)	LiCoO ₂ ^b (vol %)	LiCoO ₂ + SiO ₂ ^c (wt %)	LiCoO ₂ + SiO ₂ ^d (wt %)
LiCoO ₂	310 ± 60	190 ± 30	100.0	12	18
LiCoO ₂ /SiO ₂	350 ± 80	320 ± 100	5.03	41	57

^aMeasured with SEM. ^bCalculated from eq 2. ^cMeasured with TGA. ^dTheoretical content.

found that the presence of vapor-grown carbon fiber hindered the decomposition of PVA.

The obtained electrospun materials were observed by SEM before (Figure 3a–d) and after calcination (Figure 3e–h). Fiber mats prepared from PAA solutions with different Ce/Si mole ratios (0.06 and 0.12) were compared with references prepared from PAA solutions containing only either Ce(NO₃)₃ or SiO₂. Silica nanoparticles were visible on the fibers, creating a rough surface. The addition of Ce(NO₃)₃ resulted in reduction of the fiber diameter in comparison to the PAA/SiO₂ fiber (Table 2), which can be explained by the increase of charge density upon addition of the metal salt, inducing larger Coulombic interactions and, therefore, higher stretching of the electrospinning jet.⁴⁵ After calcination at 600 °C, the morphology of the fibers was preserved and the diameter of the fibers decreased owing to the removal of the polymer template. The incorporation of silica nanoparticles into the metal oxide fibers increased remarkably the surface area of the electrospun mats. The specific surface area of neat CeO₂ fibers was 38 m² g⁻¹, whereas it increased to 161, 155, and 127 m² g⁻¹ for SiO₂, CeO₂/SiO₂(0.12/1.00), and CeO₂/SiO₂(0.06/1.00),

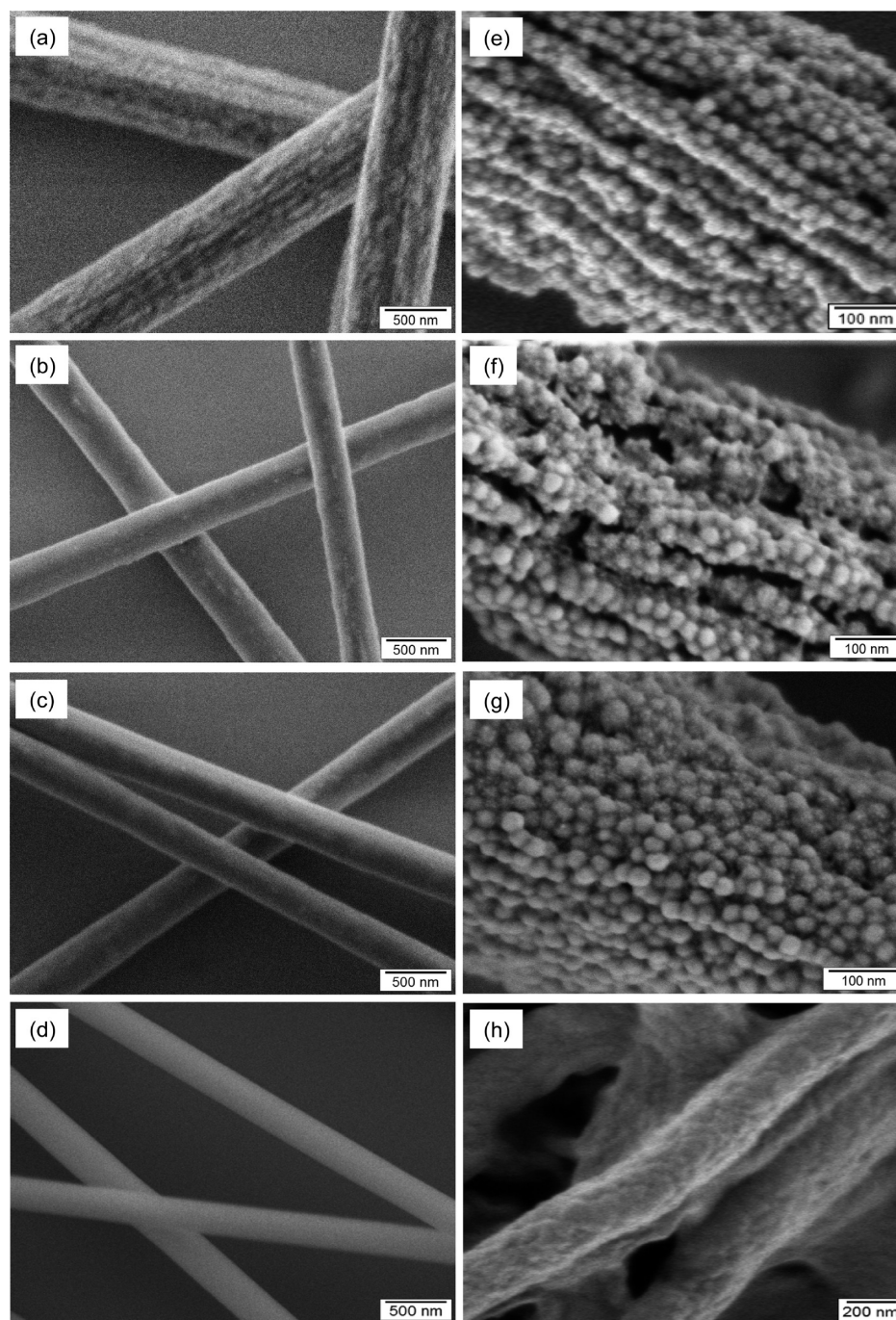


Figure 3. SEM micrographs of composite fibers as prepared: (a) PAA/SiO₂; (b, c) PAA/Ce(NO₃)₃/SiO₂ with Ce/Si molar ratios of 0.06 and 0.12, respectively, (d) PAA/Ce(NO₃)₃; and oxide fibers after calcination at 600 °C: (e) SiO₂, (f) CeO₂/SiO₂ (0.06/1.00), (g) CeO₂/SiO₂ (0.12/1.00), (h) CeO₂.

respectively. The hierarchy of size observed in the fibers (metal oxide crystallites < silica nanoparticles < fibers) is reflected in the hierarchy of porosity in the structure. Accordingly, there were two levels of porosity: the porosity created by the space between electrospun fibers, and the porosity of the silica particles, both contributing to the porosity of the resulting fibers.

The morphologies of the LiCoO₂ and LiCoO₂/SiO₂ fibers are shown in Figure 4a–c. The PAA/LiOH/Co(OH)₂ fibers before calcination were continuous, smooth, and uniform, with a diameter of 310 ± 60 nm. Similar to the CeO₂ fibers, the calcination caused shrinkage of the average fiber diameter of

LiCoO₂ to 190 ± 30 nm. LiCoO₂/SiO₂ fibers were clearly less brittle than neat LiCoO₂ fibers. Whereas the LiCoO₂ mat was converted to ultrafine pieces and powder (photograph on the top of Figure 1), the mat of LiCoO₂/SiO₂ (bottom image) remained intact after calcination. The nonwoven could be therefore handled as single object, which was not the case for the calcinated metal oxide fibers. We investigated the effect of calcination temperature on the fiber morphology. At 300 °C, a phase separation was observed on the surface of fibers (Figure 4a). The components (i.e., polymer chains, residues, and metal oxide/salt) were separated into distinct domains oriented along the surface of the fibers. This phase separation occurred

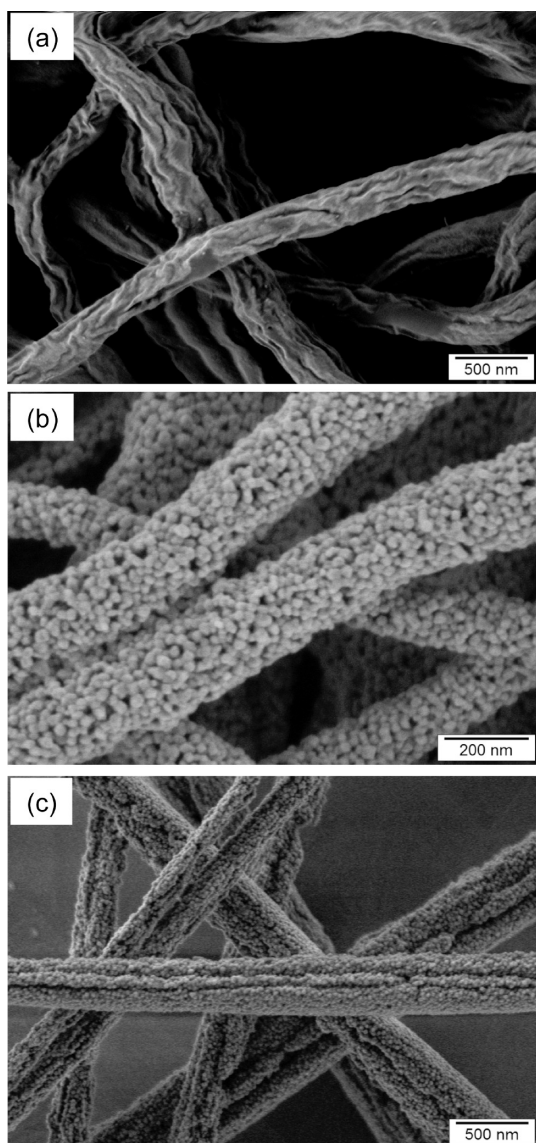


Figure 4. SEM micrographs of PAA/LiOH/Co(OH)₂ precursor fibers after calcination (a) at 300 °C, (b) at 400 °C and (c) PAA/LiOH/Co(OH)₂/SiO₂ precursor fibers calcinated at 600 °C.

uniformly on the surface along the long axis of the fiber wherein polymer-lean and polymer-rich phases were formed, indicating a spinodal decomposition. The orientation of the domains is probably a consequence of elongational electrical forces occurring during electrospinning process. When the calcination temperature was increased to 400 °C, the fibers preserved their continuous structures and the average diameter was reduced by about 40% with narrower distribution (25%). At the same time, the nucleation and growth of LiCoO₂ nanoparticles occurred and the LiCoO₂ nanoparticles were visible on the fibers surface (Figure 4b). The PAA aqueous solution composed of lithium/cobalt hydroxides was basic (pH ~9). Under this condition, surface silanols are dissociated into negatively charged oxide (Si-O⁻) on the surface. Electrostatic repulsion between negatively charged particles resulted in stable and non-aggregated silica dispersions. In the presence of silica nanoparticles of uniform size in the fibers, homogeneously assembled continuous fibers could be formed (Figure 4c).

The crystallinity of the samples was studied by X-ray diffraction (XRD). Figure 5a shows the XRD patterns of fibers

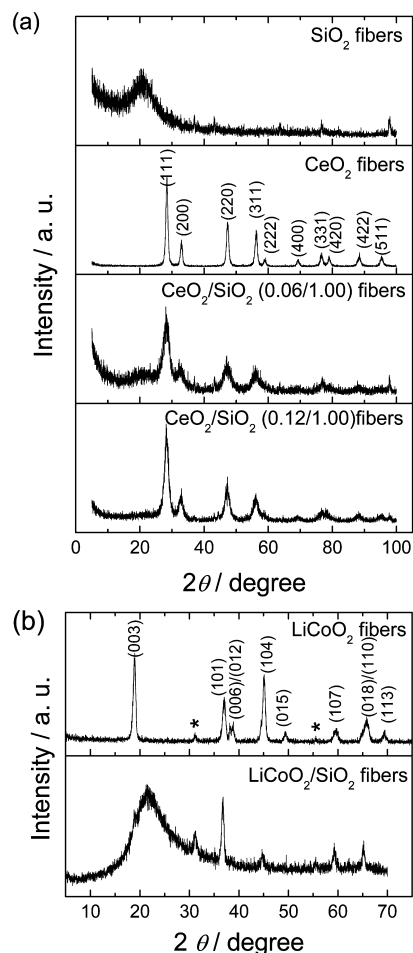


Figure 5. (a) XRD patterns of SiO₂ fibers (blank) and CeO₂ fibers prepared in the absence and presence of SiO₂ nanoparticles after calcination at 600 °C; (b) XRD patterns of lithium cobalt oxide fibers prepared in the absence and presence of SiO₂ nanoparticles after calcination at 400 °C (the stars indicate reflections of Co₃O₄).

prepared with different CeO₂/SiO₂ ratios (0.06/1.00 and 0.12/1.00) after calcination at 600 °C, compared with those of SiO₂ and CeO₂ fibers. Whereas the silica fibers displayed a typical amorphous halo, the samples containing cerium showed the characteristic reflections for cubic CeO₂ (JCPDS card No. 34–394). The increase of the amount of cerium salt resulted in sharper reflections, which correlates with the size of the crystalline domains. Under the same experimental conditions, CeO₂ fibers prepared without colloidal silica showed much narrower reflections. The sizes of the crystallites estimated by the Scherrer equation⁴⁶ from the (111) reflection were 4, 6, and 12 nm for the CeO₂/SiO₂ (0.06/1.00), CeO₂/SiO₂ (0.12/1.00) and CeO₂ fibers, respectively. These results indicate that the size of the ceria crystallites was smaller in the presence of amorphous silica and increased with increasing amount of cerium. The change in the crystallite size can be associated with the interfacial area between the colloid and the ceria salt. Because colloidal silica provides large surface area, there may be higher number of nucleation sites compared to the fibers prepared in the absence of the colloids, so that the resulting crystallites are smaller. When the amount of cerium nitrate

increased, while keeping constant the amount of the SiO₂ nanoparticles, there was no change in nucleation sites and the diameter of the particles increased.

Figure 5b contains the XRD patterns of the binary metal oxide fibers after calcination of PAA/LiOH/Co(OH)₂ in the absence and in the presence of SiO₂. In the absence of SiO₂, the diffractogram confirms the formation of LiCoO₂ (JCPDS card no. 44–0145), with a minor coexistence of Co₃O₄ (JCPDS card no. 42–1467). In the fibers formed in the presence of SiO₂ nanoparticles, the Co₃O₄ phase becomes more significant, which may be ascribed to the formation of lithiated Co₃O₄ and/or nonstoichiometric lithium cobalt oxide. The coexistence of Co₃O₄ and the formation of nonstoichiometric lithium cobalt oxides have been often reported in solid-state reaction methods from metal salts.^{47–49} A crystallite size of 14 nm was estimated by the Scherrer equation from the most intense (003) reflection for the LiCoO₂ obtained without SiO₂. The crystallite size is consistent with the particle size estimated statistically from SEM micrographs (21 ± 5 nm, Figure 4b).

The backscattered electrons detection mode of the SEM was used to localize LiCoO₂ nanoparticles among the SiO₂ (Figure 6), thanks to the atomic number contrast between both type of

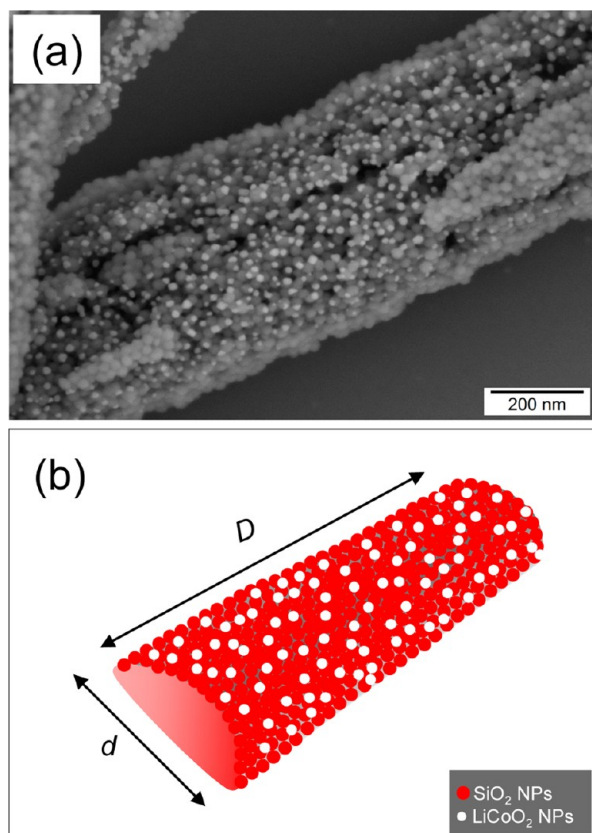


Figure 6. (a) SEM micrograph of a LiCoO₂/SiO₂ fiber obtained by calcination at 600 °C and (b) schematic representation of the simple geometrical model used to calculate percent volume of LiCoO₂/SiO₂ nanoparticles.

particles (SiO₂, and LiCoO₂). LiCoO₂ nanoparticles with a diameter of 12 ± 3 nm could be identified, being uniformly dispersed among the SiO₂ particles in the fiber. The experimental and theoretical volume percents of the particles, $V_{\text{MO[exp]}}$ and $V_{\text{MO[th]}}$, were calculated from statistical measurements of particles sizes in SEM images using eqs 1 and 2

$$V_{\text{MO[exp]}}\% = \frac{NV_{\text{p(MO)}}}{AD_{\text{SiO}_2}} \times 100 \quad (1)$$

$$V_{\text{MO[th]}}\% = \frac{V_{\text{MO}}}{V_{\text{MO}} + V_{\text{SiO}_2}} \times 100 \quad (2)$$

N represents the number of LiCoO₂ particles on the surface of a half cylinder (A), D_{SiO_2} the radius of the SiO₂ nanoparticles, and V_{p} is the volume of one spherical LiCoO₂ particle. The experimental volume percent was found to be 5.0%, which was above the theoretical value of 4.4%. Note that $V_{\text{MO[exp]}}$ represents the volume of LiCoO₂ that was observed by SEM, that is, located on the surface of the fibers. Therefore, the small difference between $V_{\text{MO[exp]}}$ and $V_{\text{MO[th]}}$ suggests that the LiCoO₂ nanoparticles are preferably situated at the fibers surface. Based in Figure 6a, we estimated that 18% of the total amount LiCoO₂ nanoparticles were present on the surface of the fibers. The fact that the surface is enriched with the metal oxide is particularly remarkable, because the metal oxide is the functional component, whereas silica plays the role of a structural framework. Such nanocomposites have potential applications as cathodes of lithium-ion batteries, functional membranes for filtration, and supported catalysts.

As a representative example, the photocatalytic activity of the CeO₂/SiO₂ fibers for the degradation of rhodamine B was investigated and compared with the SiO₂ fibers and the brittle CeO₂ fibers. The evolution of the reaction was monitored by recording the photoluminescence (PL) emission spectra of the samples at different times (Figure 7). The maximum at 580 nm decreased exponentially with respect to the irradiation time (Figure 7b). As expected, the decay of fluorescence intensity at time t over initial intensity (I/I_0) is slower for silica-supported fibers than for the neat fibers. The absolute performance of the fibers for the degradation of the dye, which is proportional to $P(\%) = 100 - (I/I_0)$, was found to increase from $P = 10\%$ (CeO₂/SiO₂:0.06/1.00) to $P = 61\%$ (CeO₂/SiO₂:0.12/1.00) when the concentration of ceria in the fibers was increased. Although P was found to be higher for the neat CeO₂ fibers (66%), the performance related to the amount of ceria in the fibers P_w are much higher for the CeO₂/SiO₂:0.12/1.00 (60% per mg of CeO₂) than for the neat CeO₂ fibers (33% per mg). This comparatively higher activity is explained by the fact that CeO₂ was well-distributed along the fibers surface, being therefore accessible for the molecules to be degraded. This result is important because the efficient use of metal oxide allows the reduction of the production costs, taking into account that SiO₂ is rather inexpensive and largely available as resource.

CONCLUSIONS

The simultaneous electrospinning of ceria and lithium cobalt oxide precursors and silica nanoparticles allows the fabrication of hierarchically structured composite nanofibers. The metal oxide was found to nucleate predominantly at the surface of the fibers during the calcination process, forming nanoparticles that were mainly present among larger silica nanoparticles on the surface of even larger fibers. This hierarchical structural organization enhanced the available surface area of the catalytically active metal oxide component and improved accordingly the efficiency of the system for catalysis, as shown by the successful degradation of a fluorescent dye by ceria fibers. Moreover, the presence of silica nanoparticles as

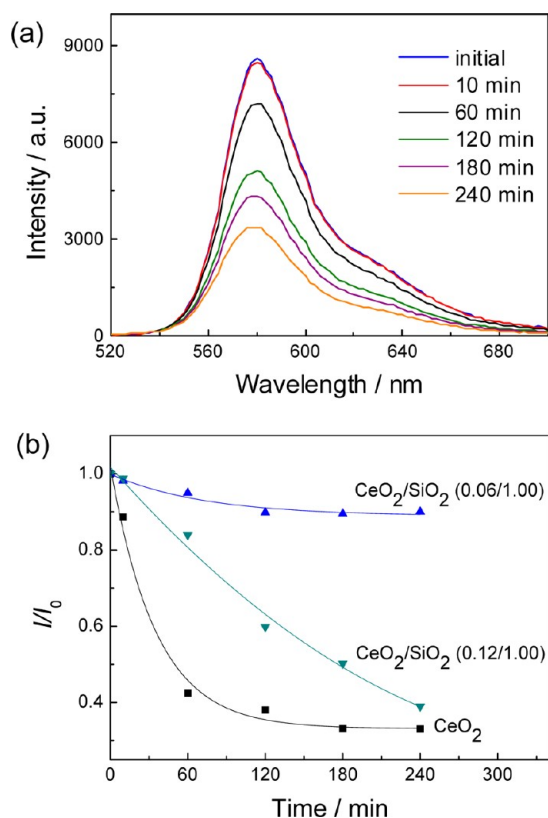


Figure 7. (a) PL emission spectra of rhodamine B solutions in the presence of $\text{CeO}_2/\text{SiO}_2$ (0.12/1.00) fibers at different time intervals, and (b) effect of different fiber catalysts on the photocatalytic degradation of rhodamine B.

structural framework for the fibers improved both thermal and mechanical stability of the nanocomposites. The conjugation of the latter features with the functionality provided by the metal oxide and the versatility of the electrospinning technique make our method extendable to a large variety of supported metal oxides.

AUTHOR INFORMATION

Corresponding Author

*Fax: +49 6131 379-100. Tel: +49 6131 379-484. E-mail: crespym@mpip-mainz.mpg.de.

Author Contributions

The manuscript was written through contributions of all authors. All authors have given approval to the final version of the manuscript.

Notes

The authors declare no competing financial interest.

ACKNOWLEDGMENTS

The authors thank Michael Steiert for XRD measurements. The financial support by the International Max Planck Research School for Polymer Materials Science (IMPRS-PMS, Mainz) is gratefully acknowledged.

REFERENCES

- (1) Choi, S. W.; Park, J. Y.; Kim, S. S. *Nanotechnology* **2009**, *20*, 1–6.
- (2) Fierro, J. L. G. In *Metal Oxides: Chemistry and Applications*, 1st ed.; Taylor and Francis: Boca Raton, FL, 2006; Vol. 2, p 32.
- (3) Kim, I. D.; Rothschild, A. *Polym. Adv. Technol.* **2011**, *22*, 318–325.

- (4) Valcarcel, V.; Souto, A.; Guitian, F. *Adv. Mater.* **1998**, *10*, 138–140.
- (5) Chen, B. J.; Sun, X. W.; Xu, C. X.; Tay, B. K. *Phys. E* **2004**, *21*, 103–107.
- (6) Yoo, S.; Dregia, S. A.; Akbar, S. A. *J. Mater. Res.* **2006**, *21*, 1822–1829.
- (7) Li, D.; Wang, Y. L.; Xia, Y. N. *Nano Lett.* **2003**, *3*, 1167–1171.
- (8) Huang, Z. M.; Zhang, Y. Z.; Kotaki, M.; Ramakrishna, S. *Compos. Sci. Technol.* **2003**, *63*, 2223–2253.
- (9) Sigmund, W.; Yuh, J.; Park, H.; Maneeratana, V.; Pyrgiotakis, G.; Daga, A.; Taylor, J.; Nino, J. C. *J. Am. Ceram. Soc.* **2006**, *89*, 395–407.
- (10) Fridrikh, S. V.; Yu, J. H.; Brenner, M. P.; Rutledge, G. C. *Phys. Rev. Lett.* **2003**, *90*, 144502–144501–144504.
- (11) Theron, S. A.; Zussman, E.; Yarin, A. L. *Polymer* **2004**, *45*, 2017–2030.
- (12) Choi, S. S.; Lee, S. G.; Im, S. S.; Kim, S. H.; Joo, Y. L. *J. Mater. Sci. Lett.* **2003**, *22*, 891–893.
- (13) Hansen, N. S.; Ferguson, T. E.; Panels, J. E.; Park, A. H. A.; Joo, Y. L. *Nanotechnology* **2011**, *22*, 1–13.
- (14) Ma, Z. J.; Ji, H. J.; Teng, Y.; Dong, G. P.; Zhou, J. J.; Tan, D. Z.; Qiu, J. R. *J. Colloid Interface Sci.* **2011**, *358*, 547–553.
- (15) Panels, J. E.; Joo, Y. L. *J. Nanomater.* **2006**, *2006*, 1–10.
- (16) Sakai, S.; Yamada, Y.; Yamaguchi, T.; Kawakami, K. *Biotechnol. J.* **2006**, *1*, 958–962.
- (17) Sakai, S.; Yamaguchi, T.; Putra, R. A.; Watanabe, R.; Kawabe, M.; Taya, M.; Kawakami, K. *J. Sol–Gel Sci. Technol.* **2012**, *61*, 374–380.
- (18) Seol, Y. J.; Kim, K. H.; Kang, Y. M.; Kim, I. A.; Rhee, S. H. *J. Biomed. Mater. Res., Part B* **2009**, *90B*, 679–687.
- (19) Ding, B.; Kim, H.; Kim, C.; Khil, M.; Park, S. *Nanotechnology* **2003**, *14*, 532–537.
- (20) Kim, Y. J.; Ahn, C. H.; Choi, M. O. *Eur. Polym. J.* **2010**, *46*, 1957–1965.
- (21) Shao, C. L.; Kim, H.; Gong, J.; Lee, D. *Nanotechnology* **2002**, *13*, 635–637.
- (22) Shi, W.; Lu, W. S.; Jiang, L. *J. Colloid Interface Sci.* **2009**, *340*, 291–297.
- (23) Chen, Y. Z.; Zhang, Z. P.; Yu, J.; Guo, Z. X. *J. Polym. Sci., Part B: Polym. Phys.* **2009**, *47*, 1211–1218.
- (24) Friedemann, K.; Corrales, T.; Kappl, M.; Landfester, K.; Crespy, D. *Small* **2012**, *8*, 144–153.
- (25) Kanehata, M.; Ding, B.; Shiratori, S. *Nanotechnology* **2007**, *18*, 1–7.
- (26) Lim, J. M.; Moon, J. H.; Yi, G. Y.; Heo, C. J.; Yang, S. M. *Langmuir* **2006**, *22*, 3445–3449.
- (27) Zhang, X. C.; Chen, Y. Z.; Yu, J.; Guo, Z. X. *J. Polym. Sci., Part B: Polym. Phys.* **2011**, *49*, 1683–1689.
- (28) Li, L.; Meyer, W. H.; Wegner, G.; Wohlfahrt-Mehrens, M. *Adv. Mater.* **2005**, *17*, 984–988.
- (29) Lu, G. Q.; Lieberwirth, I.; Wegner, G. *J. Am. Chem. Soc.* **2006**, *128*, 15445–15450.
- (30) Horzum, N.; Tascioglu, D.; Okur, S.; Demir, M. M. *Talanta* **2011**, *85*, 1105–1111.
- (31) Crespy, D.; Friedemann, K.; Popa, A. M. *Macromol. Rapid Commun.* **2012**, DOI: 10.1002/marc.201200549.
- (32) Wesselt, C.; Ostermann, R.; Dersch, R.; Smarsly, B. M. *J. Phys. Chem. C* **2011**, *115*, 362–372.
- (33) Kanjwal, M. A.; Barakat, N. A. M.; Sheikh, F. A.; Park, S. J.; Kim, H. Y. *Macromol. Res.* **2010**, *18*, 233–240.
- (34) Kanjwal, M. A.; Sheikh, F. A.; Barakat, N. A. M.; Chronakis, I. S.; Kim, H. Y. *Appl. Surf. Sci.* **2011**, *257*, 7975–7981.
- (35) Kanjwal, M. A.; Sheikh, F. A.; Barakat, N. A. M.; Li, X. Q.; Kim, H. Y.; Chronakis, I. S. *Appl. Surf. Sci.* **2012**, *258*, 3695–3702.
- (36) Strunk, J.; Vining, W. C.; Bell, A. T. *J. Phys. Chem. C* **2011**, *115*, 4114–4126.
- (37) Tang, C. J.; Zhang, H. L.; Sun, C. Z.; Li, J. C.; Qi, L.; Quan, Y. J.; Gao, F.; Dong, L. *Catal. Commun.* **2011**, *12*, 1075–1078.
- (38) Zhao, X. B.; Long, R. W.; Chen, Y.; Chen, Z. G. *Microelectron. Eng.* **2010**, *87*, 1716–1720.

- (39) Pradip; Maltesh, C.; Somasundaran, P.; Kulkarni, R. A.; Gundiah, S. *Langmuir* **1991**, *7*, 2108–2111.
- (40) Moharram, M. A.; Khafagi, M. G. *J. Appl. Polym. Sci.* **2006**, *102*, 4049–4057.
- (41) Shih, S. J.; Borisenko, K. B.; Liu, L. J.; Chen, C. Y. *J. Nanopart. Res.* **2010**, *12*, 1553–1559.
- (42) Mahmoud, W. E.; Al-Agel, F. A. *J. Phys. Chem. Solids* **2011**, *72*, 904–907.
- (43) Carewska, M.; Di Bartolomeo, A.; Scaccia, S. *Thermochim. Acta* **1995**, *269–270*, 491–506.
- (44) Mizuno, Y.; Hosono, E.; Saito, T.; Okubo, M.; Nishio-Hamane, D.; Oh-ishi, K.; Kudo, T.; Zhou, H. *J. Phys. Chem. C* **2012**, *116*, 10774–10780.
- (45) Zong, X. H.; Kim, K.; Fang, D. F.; Ran, S. F.; Hsiao, B. S.; Chu, B. *Polymer* **2002**, *43*, 4403–4412.
- (46) Langford, J. I.; Wilson, A. J. C. *J. Appl. Crystallogr.* **1978**, *11*, 102–113.
- (47) Antolini, E. *Mater. Res. Bull.* **1997**, *32*, 9–14.
- (48) Antolini, E. *Solid State Ionics* **2004**, *170*, 159–171.
- (49) Rossen, E.; Reimers, J. N.; Dahn, J. R. *Solid State Ionics* **1993**, *62*, 53–60.